Study of PET intrinsic spatial resolution and contrast recovery improvement for PET/MRI systems

2012 Phys. Med. Biol. 57 N101

(http://iopscience.iop.org/0031-9155/57/9/N101)

Phys. Med. Biol. **57** (2012) N101–N115 doi:10.1088/0031-9155/57/9/N101

NOTE

Study of PET intrinsic spatial resolution and contrast recovery improvement for PET/MRI systems

Hao Peng[1,2,3] **and Craig S Levin**[1,2,4,5]

[1] Department of Radiology, Stanford University, Stanford, CA 94305, USA
[2] Molecular Imaging Program at Stanford (MIPS), Stanford, CA 94305, USA
[3] Department of Medical Physics, McMaster University, Ontario, L8S 4K1, CANADA
[4] Department of Electrical Engineering, Stanford University, Stanford, CA 94305, USA
[5] Departmet of Physics, Stanford University, Stanford, CA 94305, USA

E-mail: penghao@mcmaster.ca and cslevin@stanford.edu

Received 11 August 2011, in final form 19 January 2012
Published 5 April 2012
Online at stacks.iop.org/PMB/57/N101

Abstract
This paper studied PET intrinsic spatial resolution and contrast recovery improvement for PET/MRI dual modality systems. A Monte Carlo simulation tool was developed to study positron diffusion in tissues with and without a magnetic field for six commonly used isotopes (^{18}F, ^{11}C, ^{13}N, ^{15}O, ^{68}Ga and ^{82}Rb). A convolution process was implemented to investigate PET intrinsic spatial resolution, taking into account three factors: positron diffusion range, collinear photon annihilation and finite detector element width. The resolution improvement was studied quantitatively as a function of magnetic field strength for three PET system configurations (whole-body, brain-dedicated and small-animal PET). When the magnetic field strength increases up to 10 T, the system spatial resolution in directions orthogonal to the field for ^{15}O, ^{68}Ga and ^{82}Rb is comparable to that of ^{18}F without the magnetic field. Beyond 10 T, no significant improvement of spatial resolution was observed. In addition, the modulation transfer function was studied to predict the intrinsic contrast recovery improvement for several existing and promising PET/MRI configurations.

(Some figures may appear in colour only in the online journal)

1. Introduction

The integration of PET and MRI has been of great interest in recent years (Marsden *et al* 2002, Zaidi *et al* 2003, Takasawa *et al* 2005, Cherry 2006, Catana *et al* 2008, Pichner *et al* 2010). Compared to PET/CT, PET/MRI has the potential to offer advantages such as superior soft tissue contrast provided by MRI, improved temporal correlation due to truly

simultaneous PET/MRI acquisition, functional–functional correlation and reduced ionizing radiation dose exposure to imaging objects. Besides, there exists another potential benefit for a combined PET/MRI scanner. In the magnetic field, the positron diffusion will be reduced due to Lorentz force on a charged particle (Iida *et al* 1986, Hammer *et al* 1994). Such effect will improve PET spatial resolution and potentially contrast recovery for small structures of interest. Several theoretical simulation and experimental studies on this topic have been carried out (Iida *et al* 1986, Wirrwar *et al* 1993, Hammer *et al* 1994, Raylman *et al* 1996).

A generalized model is desired that can analytically study the PET spatial resolution and contrast improvement inside the magnetic field for a given radioisotope and system configuration. There exist three factors limiting the intrinsic spatial resolution of a PET system: positron diffusion range, non-collinear annihilation and finite detector width (Levin and Hoffman 1999, 2000). The intrinsic spatial resolution is the convolution of resolution blurring resulting from these three factors. Other factors (i.e. block effect, inter-crystal scatter and depth of interaction) would also degrade the spatial resolution, but are not taken into account in this work, assuming that they could be removed/mitigated through advanced PET detector designs. To study the spatial resolution improvement for a PET/MRI, the reduction of positron range needs to be considered along with the other two factors. For instance, for a system where the spatial resolution is largely dominated by either the non-collinear annihilation or the finite detector width effects, the benefits merely from the positron range reduction might not be significant.

Furthermore, previous studies were mainly based on existing clinical PET system configurations (large diameter and large detector element) (Wirrwar *et al* 1993, Hammer *et al* 1994, Raylman *et al* 1996). Such configurations are significantly different from those deployed in small-animal PET systems for which the impact of the magnetic field on PET resolution would be different. Meanwhile, the PET configuration also needs to be re-engineered for a combined PET/MRI system. For instance, several PET/MRI prototypes for both preclinical and clinical applications shrink down diameters of PET rings in order to insert the PET into the MRI system (Schlemmer *et al* 2008, Catana *et al* 2008, Judenhofer *et al* 2007, 2008, Peng *et al* 2011). A small-animal PET/MRI needs to shrink the PET system's diameter from 150 down to 60 mm to locate the PET detector outside the RF coils and inside the gradient coils of a 7 T MRI scanner (Judenhofer *et al* 2008). In this context, a generalized model that could be applied for any arbitrary configuration would be preferred.

The contrast recovery for a PET system is related to its modulation transfer function (MTF), which depends on several factors including spatial resolution, specificity of radionuclides for different types of diseases and size of the object and scattered/random photons (Sorenson and Phelps 1986). In this work, the MTF was studied based upon only the intrinsic spatial resolution (i.e. point spread function, PSF), and is thus referred to as the intrinsic contrast recovery.

This work focuses on the potential spatial resolution and contrast recovery improvement due to positron range reduction in PET/MRI applications. First, a Monte Carlo package was developed for studying the positron diffusion of radionuclides without and with magnetic field. Then, the overall system spatial resolution resulting from positron range, non-collinear photon annihilation and finite detector element width was investigated quantitatively as a function of various magnetic field strengths, for three possible PET system configurations (table 1). Finally, the MTF was studied to predict the intrinsic contrast recovery improvement for a number of PET/MRI configurations.

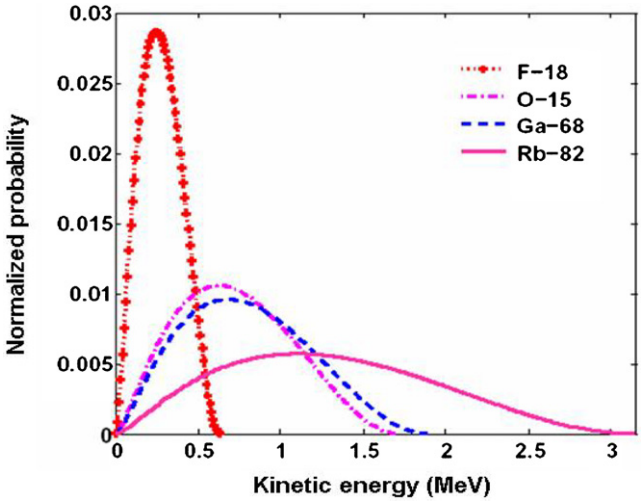

Figure 1. The theoretical distribution of positron emission energy spectra after normalization.

Table 1. Parameters of three possible PET/MRI configurations simulated (*D*: system diameter, *d*: detector width).

	D (mm)	*d* (mm)
Whole-body PET/MRI	600	4.0
Small-animal PET/MRI	60	1.5
Brain-dedicated PET/MRI	360	2.5

2. Materials and methods

We have developed a Monte Carlo simulation tool to model the diffusion of positrons within water medium. First, positrons are emitted isotropically from the origin, with the direction and energy randomly determined. After traveling a distance of fixed step size (20 μm), a positron loses a certain amount of energy to be determined by differential energy loss and cross sections for interaction within the tissue, using the continuous-slowing-down approximation (CSDA) method. Positrons are scattered during each step size. The effect of the magnetic field on positron diffusion is incorporated and for the situation without magnetic field, the magnetic field strength is set to zero. The energy, position and velocity vectors are recorded after each step. When the positron's energy is below the cutoff threshold (0.001 MeV), the simulation process terminates. Finally, the profile of positron diffusion is convolved with two other blurring factors (non-collinear photon annihilation and finite detector width) for studying the improvement of spatial resolution and contrast for three PET/MRI system configurations. The detailed simulation steps are provided in the following subsections.

2.1. Positron diffusion simulation

The energy spectrum of positron emission was analytically derived using the method previously described in Wu and Moskowski (1966) and shown in figure 1. Six commonly used isotopes (^{18}F, ^{11}C, ^{13}N, ^{15}O, ^{68}Ga and ^{82}Rb) were chosen in this study (table 2). The moving direction of positrons will be changed due to the multiple scattering. For a positron of a given energy, the scattering angle θ (relative to the direction of positron prior to the scattering) is generated from theoretical $P(\theta)$ distribution (Bethe and Ashkin 1953), as shown in formula (1). The

Table 2. Parameters of six common radioisotopes and the calculated FWHM and FWTM of positron diffusions based on fitting results using formula (4).

	E_{max} (MeV)	k_3	k_1 (mm^{-1})	k_2 (mm^{-1})	FWHM (mm)	FWTM (mm)
^{18}F	0.635	0.385	103.47	2.718	0.16 ± 0.02	1.34 ± 0.04
^{11}C	0.970	0.366	41.49	1.652	0.29 ± 0.06	2.24 ± 0.10
^{13}N	1.19	0.368	27.25	1.275	0.38 ± 0.05	2.89 ± 0.09
^{15}O	1.72	0.355	106.26	0.906	0.57 ± 0.07	4.12 ± 0.12
^{68}Ga	1.89	0.328	80.58	0.808	0.62 ± 0.07	4.61 ± 0.13
^{82}Rb	3.15	0.399	60.42	0.418	0.88 ± 0.13	8.58 ± 0.26

azimuth angle φ is randomly generated between 0 and 2π:

$$P(\theta)\,\mathrm{d}\theta = \frac{1}{\sqrt{2\pi\langle\theta^2\rangle}}\,\mathrm{e}^{\frac{-\theta^2}{2\langle\theta^2\rangle}}\,\mathrm{d}\theta$$
$$\langle\theta^2\rangle = 0.157\frac{Z(Z+1)z^2}{A}\cdot\frac{t}{(pv)^2}\cdot\log(4\pi Z^{4/3}z^2Nt(\hbar/(mv))^2), \tag{1}$$

where pv is in MeV (p is positron momentum), t is the number of atoms per square centimeter and is equal to the product of step size ($\Delta s = 20\ \mu$m) with the density of the medium. N is the number of atoms per cm^3. A and Z are the atomic weight and atomic number of the surrounding material, respectively. z is the atomic number of positron ($z = 1$). In this work, the effective values of A and Z are taken to be 14.3 and 7.23, respectively, for water.

Different from the previous work (Levin and Hoffman 1999), the positron diffusion and energy loss are studied using the CSDA method. The kinetic energy after traveling Δs in each step is given by Attix (1986)

$$E_{i+1} = E_i - \left(\frac{\mathrm{d}E_i}{\mathrm{d}x}\right)_{E_i}\cdot\Delta s, \tag{2}$$

where $(\mathrm{d}E_\mathrm{i}/\mathrm{d}x)$ is the mass collision stopping power at the energy E_i. For positrons, it can be expressed as

$$\left(\frac{\mathrm{d}E}{\rho\,\mathrm{d}x}\right)_c = k\left[\ln\left(\frac{\tau^2(\tau+2)}{2(I/(mc^2))^2}\right) + F^+(\tau) - \delta - \frac{2C}{Z}\right]$$
$$F^+(\tau) = 2\ln 2 - \frac{\beta^2}{12}\left(23 + \frac{14}{\tau+2} + \frac{10}{(\tau+2)^2} + \frac{4}{(\tau+2)^3}\right), \tag{3}$$

where $\tau = E/mc^2$, $\beta = v/c$ and $k = (0.1535Zz^2)/(A\beta^2)$. Chemical potential I is chosen to be 75 eV for water. Polarization correction δ is not included in our simulation since the medium is not in the gaseous state. For a positron with energy from 0.1 to 3.0 MeV, the contribution from shell correction ($2C/Z$) in formula (3) to the mass collision stopping power $(\mathrm{d}E_\mathrm{i}/\mathrm{d}x)$ is only ~2%–3% and therefore also not included in our simulation. The fixed step size Δs was set to be 20 μm and the cutoff energy threshold was set to 0.001 MeV. In several previous studies using the CSDA model to study positron diffusion, a step size of 100 μm was used (Iida *et al* 1986, Wirrwar *et al* 1993). As the change of positron trajectory by Lorenz force due to magnetic field occurs during each step, we expect that a finer step size would enable any effect introduced by the magnetic field to be better investigated.

In total, 10 000 positrons were generated in each simulation and the trajectories of positron diffusion in three dimensions were recorded. Then, the projection along the X/Y dimension (perpendicular to the direction of the magnetic field, i.e. Z direction) is fitted by the sum of two exponential functions which has a cusp-like shape (Derenzo 1979):

$$P(x) = k_3\,\mathrm{e}^{-k_1x} + (1-k_3)\,\mathrm{e}^{-k_2x} \quad (x > 0). \tag{4}$$

2.2. PET spatial resolution improvement

In this work, only the PET intrinsic spatial resolution for a point radiation source at the center of the system was investigated. The positron diffusion range was derived using the Monte Carlo simulation in the last section. Using the same framework previously described in Levin and Hoffman (1999), the resolution blurring caused by the non-collinear annihilation was modeled as a Gaussian distribution that is dependent on the system diameter (D) (DeBenedetti *et al* 1950); the resolution blurring caused by finite detector width was modeled as a triangular distribution that is dependent on the detector width (d). The overall PET system resolution (also referred to as PSF hereafter) is then analyzed by calculating the convolution of three blurring factors for the system configurations as shown in table 1.

^{18}F, ^{15}O,^{68}Ga and ^{82}Rb were chosen for this study, as their maximum energies typically represent the low-, medium- and high-energy range radioisotopes. In particular, ^{15}O was included due to its high relevance in PET/MRI brain studies. Three PET configurations were studied: whole-body, brain-dedicated and small-animal scanners. As to be noted later, the distribution of positron diffusion exhibits a cusp-like shape without the magnetic field, but Gaussian shape within strong magnetic fields (figures 2 to 4). Therefore, for both without and with magnetic field scenarios, the convolution study was based on the original positron diffusion trajectories instead of using fitting parameters (k_1, k_2 and k_3). By doing that, any discrepancy occurring during the fitting process can be avoided. For each positron emitter under the influence of a given magnetic field strength, five trials were simulated and used to estimate average values and uncertainties.

2.3. PET contrast improvement

The MTF can be used to quantify an imaging system's ability to recover an input contrast at a certain spatial frequency (Sorenson and Phelps 1986). A system with a flat MTF curve having a value near unity (spatial frequency) would faithfully reproduce the image object with high-contrast recovery. In PET, an object is usually sampled at a distance d that is one-third of $\mathrm{FWHM_{PSF}}$, and the highest spatial frequency component (also known as $k_{\text{Nyquist frequency}}$) to be able to be recovered is $1/(2d)$. Fourier transforms of the PSFs (without and with magnetic fields) were taken to obtain MTFs. Each MTF curve was evaluated at $k_{\text{Cutoff frequency}}$ (unit: cycles/mm). In practice, $k_{\text{Cutoff frequency}}$ is commonly set to be half of the $k_{\text{Nyquist frequency}}$ (formula 5) in order to exclude high-frequency noise components and to achieve higher signal-to-noise ratio (SNR) for the image reconstruction.

For a given radioisotope, a set of MTFs and C values were evaluated at a fixed $k_{\text{Cutoff frequency}}$, based upon the $\mathrm{FWHM_{PSF}}$ for $B = 0$ which provides the poorest contrast. Contrast improvement, defined in formula (6) is employed to study the effect of the magnetic field on contrast recovery quantitatively. C_B represents MTF values (i.e. contrast recovery) under various field strengths and $C_{B=0}$ represents MTF values without magnetic fields. Contrast improvement here is defined as the ratio between the contrast recovery inside the magnetic field and that outside the magnetic field ($B = 0$):

$$k_{\text{Cutoff frequency}} = \frac{1}{2} \cdot k_{\text{Nyquist frequency}} = \frac{3}{4 \cdot \mathrm{FWHM_{PSF}}(B=0)}, \tag{5}$$

$$\text{Contrast improvement} = \frac{C_B}{C_{B=0}}. \tag{6}$$

A set of existing and promising PET/MRI prototypes were studied. Similar to the resolution study, the results of ^{18}F,^{15}O,^{68}Ga and ^{82}Rb are presented. It should be emphasized that the MTF-based contrast recovery model proposed here predicts the achievable

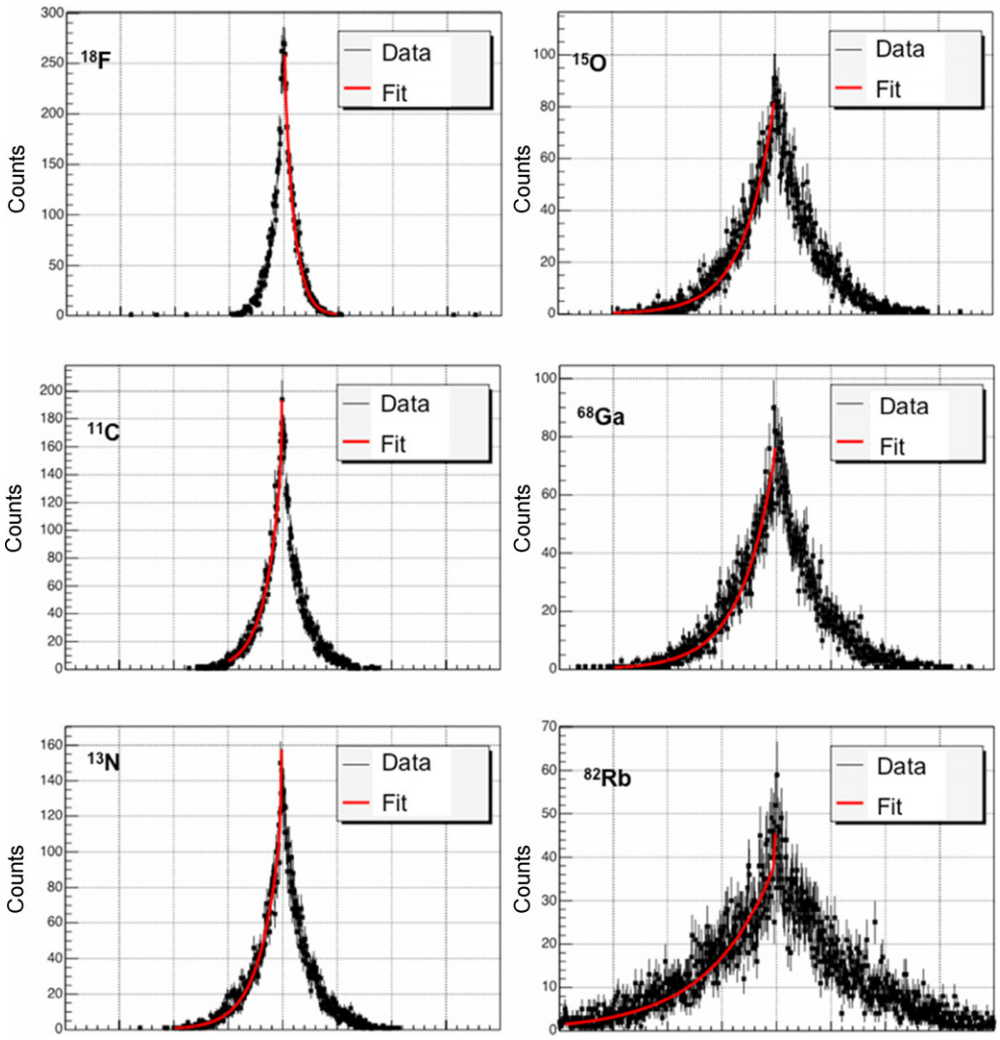

Figure 2. The 1D distribution of positron diffusion for six radioisotopes. *X*-axis represents the distance from the origin ranging from −4 to 4 mm. *Y*-axis is in counts. Total positron events $N = 10\,000$. The bin size is equal to the step size of 20 μm. See table 2 for the fitting results. The higher the energy of the radioisotope is, the larger the distance it diffuses before stopping.

contrast recovery improvement purely due to the spatial resolution improvement. It has not taken into account other factors that would also affect the contrast recovery such as non-specific tracer uptake, object size, scattering and random coincidence events in a PET system.

3. Results

3.1. Positron diffusion simulation

The 1D projection onto the *X*-axis of positron endpoints for six simulated positron emitters are shown in figure 2. Fitting parameters are listed in table 2. It is observed that the higher decay energy a positron-emitting radioinuclide has, the larger average distance the positrons will

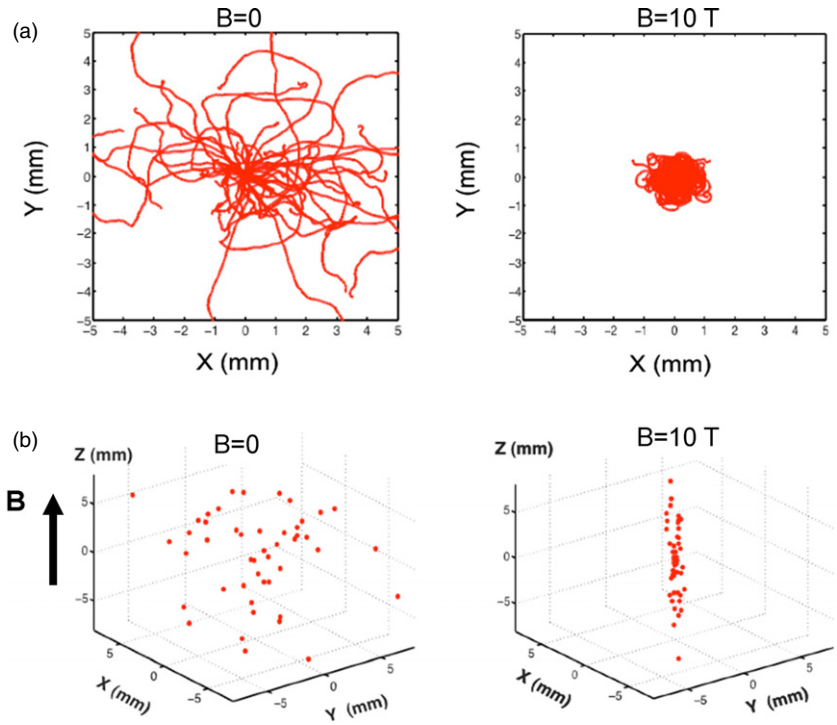

Figure 3. (a) Illustration of the lateral (orthogonal to *Z*) positron diffusion range compression inside strong magnetic fields. Radionuclide: ^{82}Rb. $N = 50$. (b) The distribution of end points in three dimensions. Positron diffusion reduction occurs only in the *X* and *Y* dimensions. The field in the simulation was applied along the *Z* direction.

diffuse (i.e. the broader distribution). Good agreement is found between our simulation results and the previous work (Levin and Hoffman 1999, 2000), where FWHM and FWTM values are 0.102/1.03 mm (^{18}F), 0.188/1.86 mm (^{11}C), 0.282/2.53 mm (^{13}N) and 0.501/4.14 mm (^{15}O) (for a positron source in a water medium). No results of ^{68}Ga and ^{82}Rb are available for comparison from the previous simulation.

A pictorial illustration of the positron diffusion with and without a strong magnetic field is shown in figure 3. The distribution of positron end points is compressed in a magnetic field of 10 T. When the magnetic field is applied along the *Z* direction, the compression only occurs orthogonal to but not along the *Z* direction. This implies that only the transaxial resolution of a PET system will be improved for a concentric PET/MRI scanner.

As the magnetic field increases above 3 T, the projections of the positron diffusion distributions transit from cusp-like (no magnetic field) to Gaussian as shown in figure 4 for ^{68}Ga and ^{82}Rb, respectively. For ^{68}Ga, the 1D positron diffusion distribution has a 1.51 $\pm$ 0.01 mm FWHM (FWTM is approximately 1.82 times FWHM) at 5 T and 0.86 $\pm$ 0.01 mm (FWHM) at 10 T. For ^{82}Rb, the corresponding FWHM values are 1.94 $\pm$ 0.02 mm at 5 T and 1.04 $\pm$ 0.01 mm at 10 T. Such transition is also observed for other four radionuclides (^{18}F, ^{11}C, ^{13}N, ^{15}O). As a result, no good *chi*-square could be obtained by fitting the distributions in the magnetic field using formula (4), and the direct comparison of FWHM and FWTM results of positron diffusion is less meaningful between situations of without and with magnetic field.

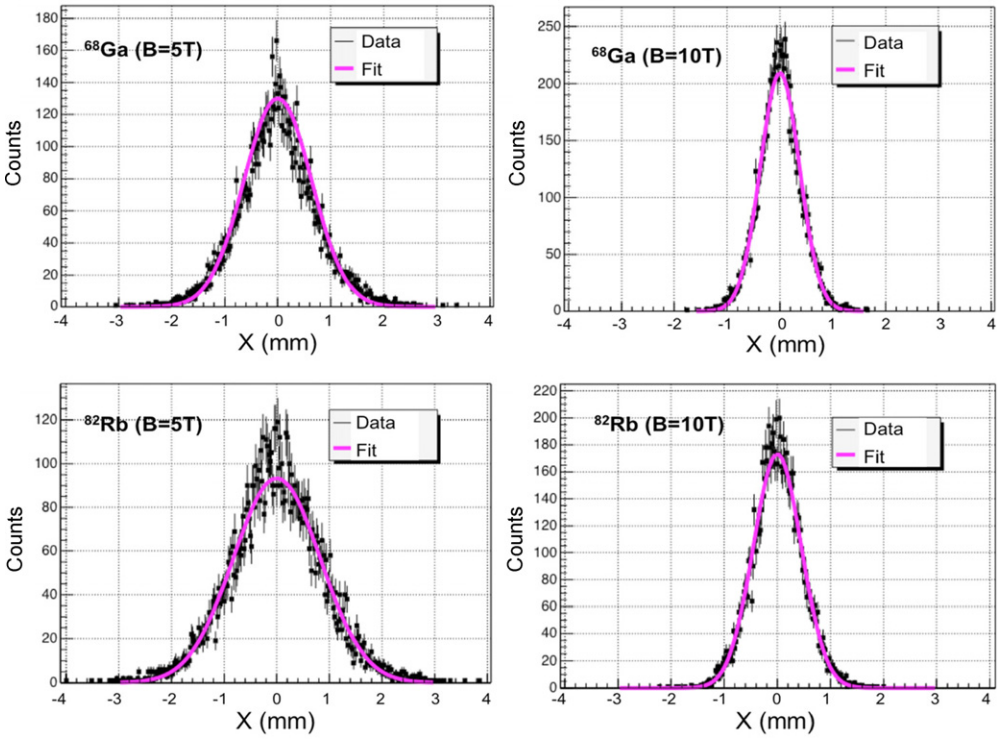

Figure 4. The 1D distribution of positron diffusion in high magnetic fields ($B = 5$ T and 10 T) for ^{68}Ga and ^{82}Rb. $N = 10\,000$ positron events. The positron diffusion distribution transitions to Gaussian shape from a cusp-like shape (figure 2 at $B = 0$).

Instead, the results of system resolution after the convolution (i.e. all have a Gaussian shape) are compared as shown in the section 3.2.

3.2. PET resolution improvement study

For illustration purposes, the convolution process for the spatial resolution study is shown in figure 5 for two PET system configurations. For small system diameter and detector size deployed in small-animal PET scanners, the contributions from three factors are quite comparable for ^{18}F (figure 5(a)). For a configuration deploying larger detector size and high positron energy emitter ^{68}Ga, the contributions from the positron range and finite detector width dominate (figure 5(b)).

Four PET system configurations were chosen for validation and the results are summarized in table 3 (Raylman *et al* 1996, Chatziioannou *et al* 1997). For all scenarios tested with our model, the convolution results exhibit Gaussian shape and thus only the FWHM result for each scenario is reported. Good agreement with previous studies indicates that our simulation is capable of producing reliable prediction of spatial resolution for arbitrary PET/MRI system configuration.

The results for a whole-body, small-animal and brain-dedicated PET scanner are shown in figure 6. The system resolution improvement was analyzed in terms of the FWHM only (i.e. due to its Gaussian shape). Besides the absolute FWHM values expressed in mm, the lateral

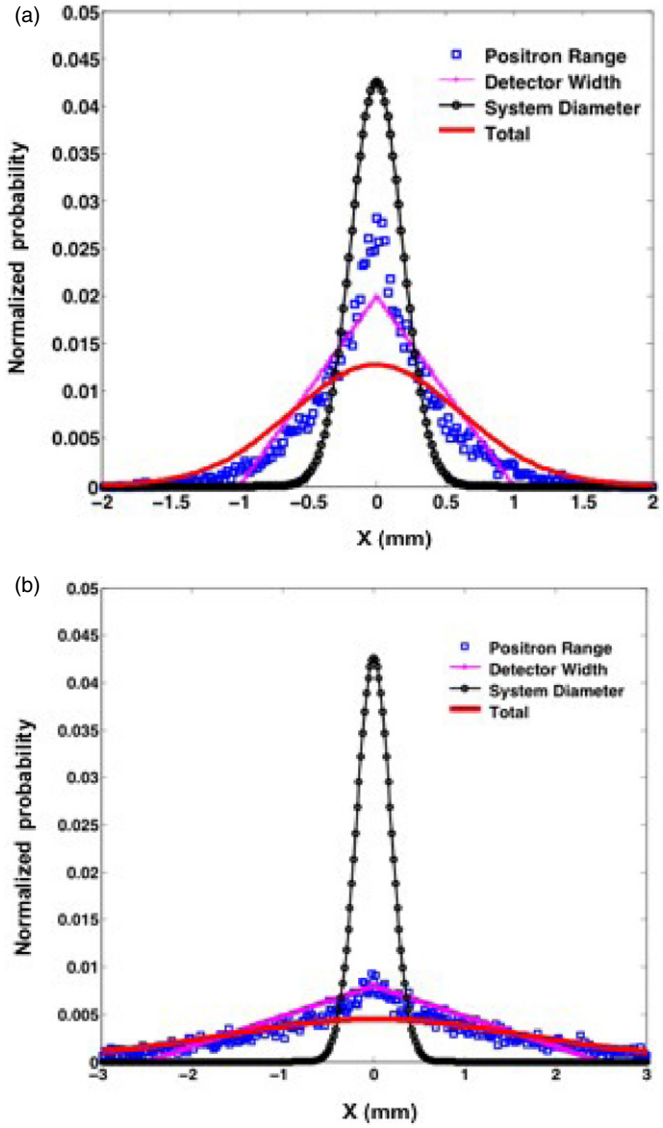

Figure 5. The resulting resolution after convolving three independent blurring effects dependent on three parameters that are referred to as the positron range, detector width and system diameter, respectively. The bin size is equal to the step size of 20 μm used in the CSDA model. (a) ^{18}F, $B = 0$ T, system diameter: 200 mm, detector width: 2 mm. (b) ^{68}Ga, $B = 0$ T, system diameter: 200 mm, detector width: 5 mm.

(orthogonal to Z) resolution improvement factor is defined as the difference between unity and relative FWHM. The relative FWHM refers to the ratio of the FWHM at certain field strength over that without magnetic fields. That said, at zero field, the relative FWHM is unity and the improvement factor is zero. The lateral resolution improvement factor defined above will be listed parenthetically for each case.

For a whole-body PET system configuration, the resolution improvement is shown in figure 6(a). For ^{18}F, the resolution is 2.69 mm FWHM at zero fields and there is no significant

Table 3. Comparison of simulation results with results in literatures (Hammer *et al* 1994, Raylman *et al* 1996). The published results with only FWHM values reported assume that the overall system resolution has a Gaussian shape. All FWHM and FWTM are presented in mm.

	D	*d*	Magnetic	Simulation results		Results in literatures	
Radioisotope	(mm)	(mm)	field (Tesla)	FWHM	FWTM	FWHM	FWTM
^{18}F	200	2	0	1.492 ± 0.004	2.78 ± 0.01	1.5	2.7
^{68}Ga	200	5	0	4.09 ± 0.03	8.14 ± 0.09	4.26 ± 0.05	
^{68}Ga	200	5	5	3.20 ± 0.02	5.61 ± 0.01	3.20 ± 0.02	
^{68}Ga	200	5	10	2.87 ± 0.01	4.90 ± 0.02	2.91 ± 0.02	

improvement below 5 T. The resolution reaches 2.58 mm FWHM (4.0%) at 10 T. For ^{15}O, ^{68}Ga and ^{82}Rb, the significant improvements occur around field strengths as low as 1.0 T. As the field strength increases, continuous resolution improvements are obtained with a gradual leveling off as the magnetic field approaches 10 T. The improvement is most significant for ^{82}Rb, which has the highest average kinetic energy. At zero field, the resolution FWHM is 5.24 mm, 3.90 mm (25.6%) at 3 T and 3.02 mm at 7 T (42.4%). For ^{68}Ga at zero field, the resolution FWHM is 3.94 mm, 3.37 mm (14.5%) at 3 T and 2.83 mm at 7 T (25.6%). The results for ^{15}O are quite comparable to ^{68}Ga as they have similar kinetic energy. The resolution FWHM is 3.76 mm ($B = 0$), 3.29 mm ($B = 3$ T, 12.5%) and 2.80 mm ($B = 7$ T, 25.5%). When the field reaches 10 T, the resolutions of other three radionuclides (^{15}O, ^{68}Ga and ^{82}Rb) are comparable to the values of ^{18}F without the magnetic field.

For a small-animal PET system configuration, the spatial resolution improvement is shown in figure 6(b). Below, the resolution results are reported for three field strengths (i.e. $B = 0$, 7, 10 T) sequentially. For ^{18}F, the resolution FWHM are 1.24 mm, 1.09 mm (12.1%) and 1.02 mm (17.7%). For ^{15}O, the resolution FWHM are 2.40 mm, 1.46 mm (39.2%) and 1.23 mm (48.7%). For ^{68}Ga, the resolution FWHM are 2.59 mm, 1.52 mm (41.3%) and 1.26 mm (51.3%). For ^{82}Rb, the resolution FWHM are 4.11 mm, 1.82 mm (55.7%) and 1.43 mm (65.2%), which is the most significant improvement for all studied scenarios.

For a brain-dedicated PET system configuration, the system spatial resolution improvement shown in figure 6(c) exhibits the same pattern as the other two system configurations. The simulation results are reported for three field strengths (i.e. $B = 0$, 3 T, 7 T) sequentially. For ^{18}F, the resolution FWHM are 1.83 mm, 1.79 mm (2.2%) and 1.69 mm (7.6%). For ^{15}O, the resolution FWHM are 2.96 mm, 2.55 mm (15.2%) and 1.98 mm (33.3%). For ^{68}Ga, the resolution FWHM are 3.15 mm, 2.64 mm (16.2%) and 2.03 mm (35.6%). For ^{82}Rb, the resolution FWHM are 4.57 mm, 3.25 mm (28.8%) and 2.28 mm (50.1%). The extent of resolution improvement exhibited here is in between that observed for the whole-body and small-animal configurations stated above.

3.3. PET contrast improvement study

An illustration of MTFs dependence as a function of magnetic field strengths is shown in figure 7. When the spatial resolution improves (i.e. a narrower PSF) as the magnetic field increases, the MTFs get broader accordingly. For ^{82}Rb and the small-animal system configuration described above, the MTFs for three field strengths ($B = 0$, 3 and 10 T) are shown. The FWHM_{PSF} values are 4.11, 3.1 and 1.43 mm ($B = 0$, 3, 10 T), respectively. $k_{\text{Cutoff frequency}}$ is set to be (3/4)*(1/4.11) = 0.183 (cycles mm^{-1}).

The contrast improvement defined in formula (6) for different PET/MRI configurations is shown in figure 8. For the small-animal system configuration, the contrast improvement

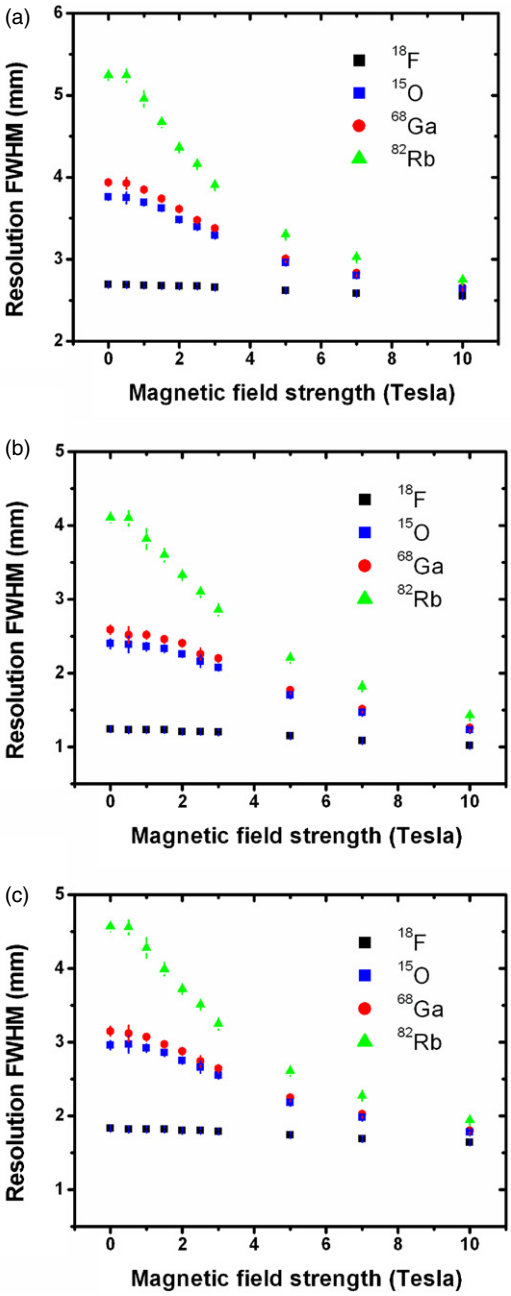

Figure 6. The system spatial resolution as a function of magnetic field strengths for a whole-body (a), small-animal (b) and brain-dedicated (c) PET system configuration. The spatial resolution shows reduction for all three cases. For ^{18}F, a slight improvement is observed only when the field strength exceeds 5 T. For ^{15}O,^{68}Ga and ^{82}Rb, a continuous system improvement is obtained from the magnetic field of 1 T while gradually leveling off as the field approaches 10 T.

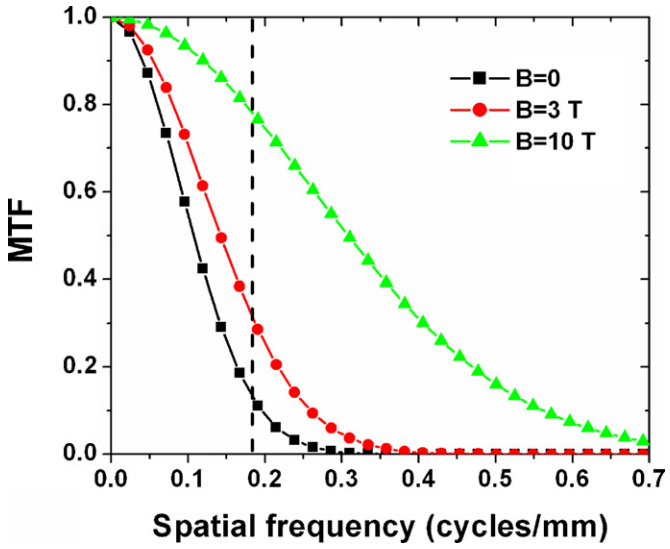

Figure 7. The MTF for a small animal PET/MRI system configuration under three magnetic field strengths. Radionuclide: ^{82}Rb. The spatial resolution (FWHM$_{PSF}$) is 4.11 mm ($B = 0$), 3.1 mm ($B = 3$ T) and 1.43 mm ($B = 10$ T). The vertical dotted line represents the cutoff frequency based on FWHM$_{PSF}$ ($B = 0$), which is $(3/4)^*(1/4.11) = 0.183$ cycles/mm. Improved spatial resolution in strong magnetic fields results in better contrast recovery at a given spatial frequency.

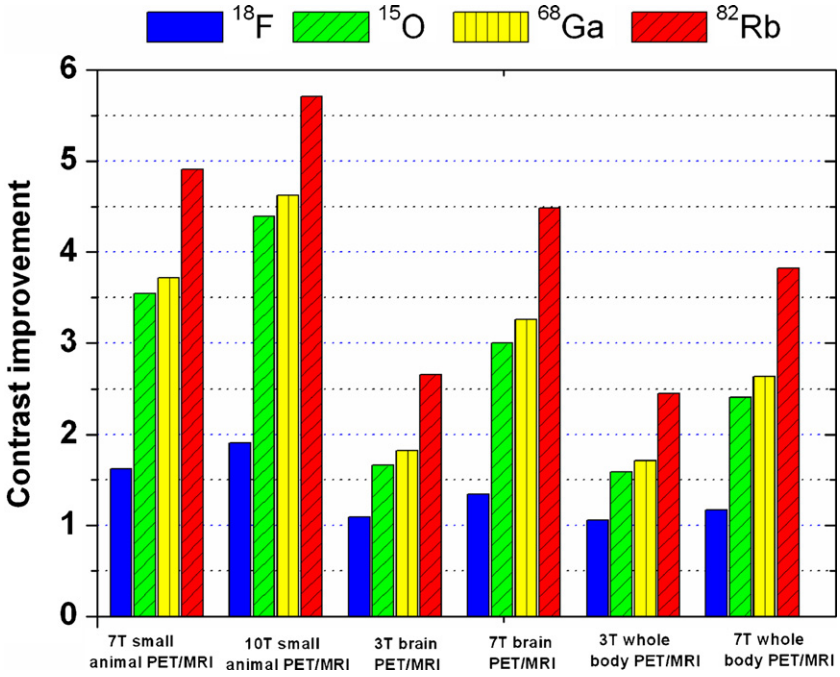

Figure 8. The contrast improvement (formula 12) for existing and possible PET/MRI prototypes, assuming each system has a cutoff frequency that is equal to the half of the Nyquist frequency (based on FWHM$_{PSF}$ in FBP image reconstruction).

is 1.62 (^{18}F), 3.54 (^{15}O), 3.72 (^{68}Ga) and 4.91 (^{82}Rb) at 7 T, and 1.91 (^{18}F), 4.39 (^{15}O), 4.62 (^{68}Ga) and 5.51 (^{82}Rb) at 10 T. For the brain system configuration, the contrast improvement is 1.09 (^{18}F), 1.66 (^{15}O), 1.82 (^{68}Ga) and 2.66 (^{82}Rb) at 3 T, and 1.34 (^{18}F), 3.00 (^{15}O), 3.26 (^{68}Ga) and 4.48 (^{82}Rb) at 7 T. For the whole-body system configuration, the contrast improvement is 1.06 (^{18}F), 1.59 (^{15}O), 1.71 (^{68}Ga) and 2.45 (^{82}Rb) at 3 T, and 1.17 (^{18}F), 2.41 (^{15}O), 2.64 (^{68}Ga) and 3.82 (^{82}Rb) at 7 T.

4. Discussion

4.1. Positron diffusion simulation

It is observed that the positron range results previously reported (Levin and Hoffman 1999, 2000) are consistently lower when compared to our results for the same radionuclides. This can be attributed to the fact that the CSDA model was used in our study and a fixed position increment (step size) was employed when considering the energy loss and scattering of positrons, while in the previous work done by Levin and Hoffman, a full model of the different types of interactions encountered by positrons traversing matter such as multiple Coulomb scatter off the nucleus, ionization and excitation, and delta electron production was employed rather than assuming that the positron follows a diffusion model and continuously slows down. In addition, the history of all interactions between positron and the medium was calculated by assuming a fixed energy loss step in the previous work rather than a fixed position increment. Therefore, these two models exhibit a slight difference toward the end of the positron trajectories (lower energy), where large angle scattering is more likely to occur (formula 1) and positrons lose most of their energy as $\mathrm{d}E_i/\mathrm{d}x$ rapidly increases with decreasing velocity (formula 2). Essentially, the non-diffusion-based model provides finer sampling to study the kinetics of the positron migration process than CSDA approximation as a positron approaches the end of its track (lower energy).

When a high magnetic field is applied, the positron diffusion range is reduced (figures 3 and 4). In addition, the distribution transitions from a cusp-like shape to a more Gaussian shape as the field increases. The Gaussian shape of positron diffusion distribution in magnetic fields of 5 and 9.4 T has been previously reported (Hammer *et al* 1994, Raylman *et al* 1996). A possible explanation for the shape transition is provided here. Inside magnetic fields, a positron is subjected to the Lorenz force and its trajectory will change from a straight line to the spiral curve. The radius of such a spiral curve is proportional to the positron energy. In other words, the trajectory change due to the magnetic field is more significant for positrons of lower energy compared to that of positrons of higher energy, assuming that the fixed step size is being used. For the cusp-like distribution without a magnetic field, those end points contributing to the tails represent positrons emitted with higher kinetic energy that can travel longer distances. They are subjected to less energy loss in the early stage of their diffusion processes but larger energy loss as they approach the end. Consequently, the magnetic field affects their trajectories more effectively (i.e. smaller radius) in the later stage where positrons have less energy. Thus, in the presence of a magnetic field, the long tails tend to diminish and the distribution becomes more Gaussian in shape.

4.2. PET spatial resolution and contrast recovery improvement

We investigated the resolution improvement as a function of magnetic field strength for three PET system configurations (figure 6). For low decay energy radioinuclides such as ^{18}F, the improvement effect is very marginal and significant improvement only emerges once the field

strength exceeds 5 T. For other low decay energy radionuclides such as ^{11}C and ^{13}N, one would expect to see a similar dependence on magnetic field strength as ^{18}F. For medium and high-energy radioisotopes such as ^{15}O,^{68}Ga and ^{82}Rb with the larger average positron range, significant improvements occur for fields as low as 1.0 T and continue all the way up to 10 T. In a high magnetic field of 10 T, the system spatial resolutions of ^{15}O,^{68}Ga and ^{82}Rb are quite comparable to that of ^{18}F without the magnetic field for all three configurations.

Associated with the resolution improvement, PET/MRI may also result in contrast improvement (figure 8). Such contrast improvement would improve image quality in two ways. First, if a PET system designer/user keeps the spatial sampling unchanged even with high magnetic field applied (i.e. better spatial resolution is not necessary) and the total statistics are the same, the reconstructed image would have a higher SNR within strong magnetic fields than that without magnetic fields. Alternatively, the total statistics (i.e. injected dose or total imaging time) can be reduced accordingly to maintain the same SNR with benefits such as reduced radiation doses and shorter scan time. Second, when the magnetic field is present, a PET system designer/user can choose to increase the sampling (i.e. higher spatial frequency) to achieve better spatial resolution while not necessarily requiring significant increase in statistics. The reason is that as a PSF sharpens, the total statistics inside the PSF curve remain the same. Consequently, the SNR inside each image pixel determined by Poisson counting statistics will also remain the same. To put it another way, for those situations where the PSF is not sharper, eight times more counts are required to maintain the same SNR when the pixel size in a PET image is reduced by a factor of 2 (Sorenson and Phelps 1986). Furthermore, the general model proposed here would be able to predict the PSF at the isocenter of a PET/MRI system. This might be used to derive the system matrix kernel to be incorporated into statistical PET image reconstruction algorithms (Panin *et al* 2006).

The positron range is a significant contributor to PET resolution for high decay energy isotopes, especially for small-animal imaging systems where the blurring from non-collinearity and detector width is not significant. Due to both spatial resolution and contrast recovery improvement, PET/MRI systems may enable the detection of smaller lesions, more accurate delineation between closely spaced pathological structures and mitigation of the partial volume effect in quantitative PET studies (Hoffman *et al* 1982, Mazziotta *et al* 1981, Donahue *et al* 2006). In addition, PET/MRI may allow the evaluation and increased use of new pharmaceuticals of high decay energy isotopes, such as ^{68}Ga-labeled guanine using ethylenedicysteine for assessing tumor proliferation (Kurihara *et al* 2007), and ^{82}Rb for rest/stress paired studies in cardiac perfusion imaging (Nakazato *et al* 2011).

Acknowledgments

The authors would like to thank Dr Blain Chronik at the University of Western Ontario, Canada for useful discussion. This work was supported in part by the Dean's Postdoctoral Fellowship, School of Medicine, Stanford University.

References

Attix F H 1986 *Introduction to Radiological Physics and Radiation Dosimetry* (New York: Wiley-Interscience)

Bethe H A and Ashkin J 1953 *Experimental Nuclear Physics* (New York: Wiley)

Catana C *et al* 2008 Simultaneous *in vivo* positron emission tomography and magnetic resonance imaging *Proc. Natl Acad. Sci. USA* **105** 3705–10

Chatziioannou A, Cherry S R, Shao Y, Silverman R W, Meadors K, Farquhar T and Phelps M E 1997 MicroPET I: performance evaluation of a very high resolution PET scanner for imaging small animals *J. Nucl. Med.* **7** 1164–75

Cherry S R 2006 Multimodality *in vivo* imaging systems: twice the power or double the trouble? *Annu. Rev. Biomed. Eng.* **8** 35–62

DeBenedetti S, Cowan C E, Konneker W R and Primakoff H 1950 On the angular distribution of two-photon annihilation radiation *Phys. Rev.* **77** 205–12

Derenzo S E 1979 *Precision measurement of annihilation point spread distributions for medically important positron emitters Positron Annihilation* ed R R Hasiguti and K Fujiwara (Sendai, Japan: The Japan Institute of Metals) pp 819–23

Donahue M J *et al* 2006 An account of the discrepancy between MRI and PET cerebral blood flow measures. A high-field MRI investigation *NMR Biomed.* **19** 1043–54

Hammer B E, Christensen N L and Heil B G 1994 Use of a magnetic field to increase the spatial resolution of positron emission tomography *Med. Phys.* **21** 1917–20

Hoffman E J, Huang S C, Plummer D and Phelps M E 1982 Quantitation in positron emission computed tomography: 6. Effect of nonuniform resolution *J. Comput. Assist. Tomogr.* **6** 987–99

Iida H *et al* 1986 A simulation study of a method to reduce positron annihilation spread distributions using a strong magnetic field in positron emission tomography *IEEE. Trans. Nucl. Sci.* **33** 597–600

Judenhofer M S *et al* 2007 PET/MR images acquired with a compact MR compatible PET detector in a 7-T magnet *Radiology* **244** 807–14

Judenhofer M S *et al* 2008 Simultaneous PET-MRI: a new approach for functional and morphological imaging *Nature Medicine* **14** 459–65

Kurihara H *et al* 2007 Ga-68-EC-guanine for PET assessment of cell proliferative activity *J. Nucl. Med.* **48** 1264–71

Levin C S and Hoffman E J 1999 Calculation of positron range and its effect on the fundamental limit of positron emission tomography system spatial resolution *Phys. Med. Biol.* **44** 781–99

Levin C S and Hoffman E J 2000 Calculation of positron range and its effect on the fundamental limit of positron emission tomography system spatial resolution *Phys. Med. Biol.* **45** 559 (corrigendum)

Marsden P K *et al* 2002 Simultaneous PET and NMR *Br. J. Radiol.* **75** 53–9

Mazziotta J C, Phelps M E, Plummer D and Kuhl D E 1981 Quantitation in positron emission computed tomography: 5. Physical–anatomical effects *J. Comput. Assist. Tomogr.* **5** 734–43

Nakazato R *et al* 2011 Diagnostic accuracy of quantitative Rubidium-82 positron emission tomography myocardium perfusion imaging: validation within invasive coronary angiography *J. Am. College Cardiol.* **57** 652–9

Panin V Y, Kehren F, Michel C and Casey M E 2006 Fully 3D PET reconstruction with system matrix derived from point source measurements *IEEE Trans. Med. Imaging* **25** 907–21

Peng H, Olcott P D, Spanoudaki V and Levin C S 2011 Investigation of a clinical PET detector module design that employs large-area avalanche photodetectors *Phys. Med. Biol.* **56** 3603–27

Pichner *et al* 2010 PET/MRI: paving the way for the next generation of clinical multimodality imaging applications *J. Nucl. Med.* **51** 333–6

Raylman R R, Hammer B E and Christensen N L 1996 Combined MRI–PET scanner: a Monte Carlo evaluation of the improvements in PET resolution due to the effects of a static homogeneous magnetic field *IEEE Trans. Nucl. Sci.* **43** 2406–12

Schlemmer *et al* 2008 Simultaneous MR/PET imaging of the human brain: feasibility study *Radiology* **248** 1028–35

Sorenson J and Phelps M E 1986 *Physics in Nuclear Medicine* 2nd edn (New York: Saunders) pp 367–9

Takasawa M *et al* 2005 How reliable is perfusion MR in acute stroke?: validation and determination of the penumbra threshold against quantitative PET *Stroke* **39** 870–7

Wirrwar A *et al* 1993 4.5 Tesla magnetic field reduces range of high-energy positrons-potential implications for positron emission tomography *IEEE Trans. Nucl. Sci.* **44** 184–9

Wu C S and Moskowski S A 1966 *Beta Decay* (New York: Interscience)

Zaidi H, Montandon M L and Slosman D O 2003 Magnetic resonance imaging-guided attenuation and scatter corrections in three-dimensional brain positron emission tomography *Med. Phys.* **30** 937–48